MTLA 42 (2025) 102483

Contents lists available at ScienceDirect

Materialia

journal homepage: www.elsevier.com/locate/mtla

Full Length Article

Deformation mechanisms of nanoporous flexible transparent electrodes based on particle-free silver inks

Oleksandr Glushko [a,*], Michael Hengge [b], Konstantin Livanov [c], Natalia Zamoshchik [c], Emil J.W. List-Kratochvil [b,d], Felix Hermerschmidt [d]

[a] Department of Materials Science, Montanuniversität Leoben, 8700 Leoben, Austria
[b] Helmholtz-Zentrum Berlin für Materialien und Energie, Hahn-Meitner-Platz 1, 14109 Berlin, Germany
[c] OrelTech GmbH, Rudower Chaussee 29, 12489 Berlin, Germany
[d] Humboldt-Universität zu Berlin, Institut für Physik, Institut für Chemie, IRIS Adlershof, Zum Großen Windkanal 2, 12489 Berlin, Germany

ARTICLE INFO

Keywords:
MOD inks
Transparent flexible electrode
Nanoporous
Digital image correlation, In-situ resistance
Fatigue

ABSTRACT

In this work, we explore the relationships between the morphology, deformation behavior, and functionality of transparent electrodes based on metal-organic decomposition (MOD) silver inks on PET substrates. A self-organized nanoporous microstructure with good interconnectivity of silver ligaments is shown to provide the necessary optical transparency and sufficient conductivity of the electrode. Tensile tests with in-situ resistance measurements revealed moderate resistance increase with increasing applied strain, indicating the suitability of the coatings for flexible electronics applications. With the help of in-situ scanning electron microscopy in combination with digital image correlation, it is demonstrated that cracks which are generated during a tensile test are short and isolated, which is beneficial for good electromechanical stability during monotonic and cyclic loading. In contrast to alternative methods for synthesis of nanoporous ultrathin films, the demonstrated transparent electrode is fabricated by a single printing-curing process under very low consumption of particle-free MOD ink, thus being suitable for cost-effective mass production.

1. Introduction

In recent years, flexible electronic devices have become increasingly present in research and industry. Replacing rigid glass substrates by polymer foils gives not only mechanical flexibility to displays [1,2], touchscreens [3], sensors [4,5], photovoltaics [6] etc., but allows to make them thin and lightweight, simultaneously enabling cost-effective large-area production. A particular challenge in the development of flexible optoelectronic devices is the material choice for transparent conductors. While today's de facto standard material for transparent electrodes – indium tin oxide (ITO) [7] – can be readily applied onto flexible substrates like polyethylene terephthalate (PET), its inherent brittleness severely limits its use in applications where it is subjected to mechanical stress [8]. Moreover, indium belongs to the category of critical raw materials, i.e. a raw material whose supply might become limited in the near future, according to the European Commission [9]. Therefore, the replacement of indium-based transparent conductors with more reliable and abundant materials has been a continued focus of materials research and development. Multiple alternative approaches enabling fabrication of ITO-free flexible transparent electrodes have been suggested in literature, including ultrathin metal films sandwiched between oxide films [10–12], regular metal grids [13–15], random metal nanowire networks [16–19], or nanostructured metal films [20–23]. We refer the reader to recent reviews [11,24–26] for more details.

Despite the variety of technological approaches enabling effective fabrication of ITO-free transparent conductors in the lab, critical limitations appear during scaling up the technology, particularly when large-area mass production is pursued. For instance, vacuum-based physical vapor deposition (PVD) is required for ultrathin oxide-metal-oxide sandwiches; fabrication of regular metal grids is time-consuming on a large scale; solutions containing nanowires or nanotubes are too costly; nanostructured films require multiple lithographic steps. For large-area roll-to-roll production, cost-effective solution-processed materials which require just printing and curing steps are required.

Particle-free solutions based on metal-organic decomposition (MOD) inks have the potential to satisfy these requirements. The MOD inks consist of oxidized metallic precursors, such as metal salts or organo-

* Corresponding author.
E-mail address: oleksandr.glushko@unileoben.ac.at (O. Glushko).

https://doi.org/10.1016/j.mtla.2025.102483
Received 18 March 2025; Accepted 9 July 2025
Available online 10 July 2025

metallic complexes, dissolved in suitable solvents along with stabilizers [27,28]. After printing, the curing process decomposes the organic ligands and reduces the precursors to a metallic film [27–30]. Currently, silver and copper are the most employed materials, but MOD inks with gold and even aluminum have been reported as well [18,31–34]. Recently also advanced electronic materials, like transition-metal dichalcogenide MoS_2, were successfully printed on polymer substrate using a particle-free ink [35].

For flexible electrodes, the choice of metal may firstly depend on the desired work function within the device. While silver offers excellent electrical conductivity, it is not suitable for all applications. In particular, silver is incompatible with perovskite-based solar cells and LEDs due to chemical reactions that degrade device stability [36], making gold a more appropriate choice in this case. Furthermore, the metallization process is very sensitive to oxidization and therefore requires inert conditions with only minimal oxygen present. Although gold is more expensive, it is more resistant to oxidation and thus easier to process for stable electrodes. In terms of cost, copper can be utilized as a cheaper material, being roughly 65 times cheaper than silver. However, oxidation of Cu nanoparticles must be strictly controlled [37].

In general, particle-free inks possess a longer shelf life than traditional nanoparticle-based inks, while simultaneously preventing the clogging of nozzles and print heads [27]. Moreover, since there is no need to first produce nanoparticles or nanowires, cap them with protective layers and then remove them after deposition, the processes of fabricating and curing the particle-free ink are simplified. Therefore, particle-free MOD inks are potentially more cost-effective and energy-efficient with respect to mass production [38].

Although MOD inks are mostly utilized for production of regular opaque conductors [27,39], it was recently demonstrated that ultrathin layers of cured MOD inks possess the necessary combination of optical transparency and electrical conductivity to act as a transparent electrode in a flexible OLED device [30,40]. Fabrication of such electrodes benefits from the advantages of MOD inks and, at the same time, only requires a single printing-curing procedure without additional nanofabrication steps.

Apart from sufficient optical transparency and electrical conductivity, the additional requirement for flexible electronics is the stability during mechanical loading. Although mechanical behavior of PVD films on polymer substrates is described well [41–43], understanding of the deformation and fracture mechanisms in novel transparent electrode types is very poor. Typically, the flexibility is proved by applying various numbers of bending cycles using custom-made setups (or even manually) and demonstrating that no significant reduction of electrical conductivity is observed. For reliable production and functioning of future flexible devices, mechanical behavior of transparent electrodes must be better understood in terms of the underlying mechanism of deformation and fracture. Specifically, in the case of multi-component, nanostructured, or ultrathin layers, the deformation mechanisms are different from those in continuous PVD films and must be considered at small scale.

Therefore, this work provides a detailed analysis of the morphology and structure of nanoporous transparent electrodes based on MOD inks, considers their deformation behavior at the nanoscale, and describes their electrical degradation during monotonic and cyclic mechanical loading. The combination of different in-situ methods enabled establishment of solid correlations between the topological and electrical evolution induced by monotonic and cyclic mechanical strain. For the sake of comparison, the same analysis was also applied to a thick, low-resistance nanoporous conductive layer obtained from the same printing-curing process.

2. Materials and methods

2.1. MOD ink formulations, properties, printing, and metallization

The two plasma metallization inks used in this study are commercial products OTech T 1053 and OTech Jet 1151, provided by OrelTech GmbH. Both inks contain an organometallic precursor that includes Ag^+ ions in addition to a combination of organic solvents that facilitate inkjet printing and the subsequent metallization process [44]. While precise ink formulations and manufacturing processes are commercial secrets, both OTech T 1053 and OTech Jet 1151 inks contain common, hydrophilic solvents from the glycol, alcohol, and ketone families that assist in dissolving metal precursors and in making the inks shelf-stable and suitable for the chosen ink application method. The choice of solvents and the concentration of the metal precursor in each case are dictated by the target metal layer thickness, the desired metal crystal shape, and the ink's physical parameters. Specifically, the ink viscosity of both inks, measured using an Ostwald (U-tube glass capillary) viscometer, was ensured to be in the range of 10-12 cP at room temperature. Surface tension, assessed by the drop weight method, was adjusted to be in the range of 25–30 mN m^{-1} at room temperature. These liquid parameters fulfill the necessary requirements for the use of the ink in inkjet printing. Upon contact with RF plasma, the silver cations undergo reduction to the Ag^0 state. Due to the simultaneous plasma-assisted decomposition of the organic solvents, the resulting metallic particles assemble into polycrystalline layers. This process has been described in more details in previous research [40,45,46].

PET substrates with a thickness of 100 μm were sonicated in DI water and isopropanol for 5 minutes and thoroughly dried under a nitrogen flow. Prior to printing, the substrates were activated for 3 minutes using a Diener Pico low-pressure plasma cleaner system with argon plasma at a gas flow of 30 sccm and power of 150 W. This step ensured good wetting of the ink on the substrates.

Inkjet printing was carried out using an off-the-shelf Epson XP-235 printer. Both inks were loaded into single-use cartridges. In the case of OTech T 1053, "gray" RGB parameters (40, 40, 40) were employed to print 15 × 10 cm rectangles with a 600 dpi resolution. In the case of OTech Jet 1151, "black" RGB parameters (0, 0, 0) were used to print 15 × 10 cm rectangles with the same resolution of 600 dpi.

Ink curing was performed in a Diener Pico plasma cleaner system immediately after printing. After the chamber pressure was stabilized at 0.4 mbar, argon plasma at a gas flow of 20 sccm and power of 150 W was used to completely reduce the printed layers to metal. In all cases, the processing time inside the plasma chamber was 5 minutes, after which no organic solvents remained, and the layer was fully metallic. Printed OTech T 1053 ink resulted in a transparent polycrystalline silver layer with a nominal thickness of 30 nm, as determined gravimetrically and further assessed in previous work [40]. Printed OTech Jet 1151 ink resulted in an opaque polycrystalline silver layer with a nominal thickness of 150-200 nm, as determined gravimetrically. Throughout this paper, the transparent 30 nm thick coatings will be referred to as "transparent" samples, while the thicker opaque films will be referred to as "low-resistance" samples.

2.2. Characterization methods

The sheet resistance of the as-deposited layers on the PET substrates was measured on an approximately 5 × 5 cm^2 coated area in van der Pauw geometry, using a Keithley 2400 SourceMeter as a current source and a Keithley 2000 as a voltmeter.

SEM characterization was performed in a Zeiss Leo 1525 scanning electron microscope.

Optical transmission spectra were collected with a Perkin Elmer Lambda 950 double-beam spectrometer against a blank reference in 1 nm steps.

Uniaxial tensile tests were performed with an MTS Tytron 250

universal tensile tester in displacement-controlled mode using 4 × 40 mm^2 samples. The initial gauge length of the samples was 20 mm, and a displacement rate of 5 μm s^{-1} was applied, giving the resulting strain rate of 2.5 × 10^{-4} s^{-1}. The maximum applied strain was 10%, and at least three samples of each type were tested. The electrical resistance was measured in four-point probe geometry in-situ during straining, with the electrical contacts incorporated directly into the grips. A digital multimeter (Keithley 2000) was used to measure the resistance values which were communicated to a computer through an RS232 port. Cyclic (fatigue) tests were performed in the same configuration by applying a sine strain function with a period of 2 s (i.e. 0.5 Hz) with the minimum value of zero strain and maximum value of either 1% or 2%. The choice of the strain levels for monotonic and cyclic loading corresponds to the potential applications in the field of flexible or lightweight electronics.

For digital image correlation (DIC), the low-resistance samples were strained in-situ inside the SEM Zeiss Leo 1525 using a custom-made compact manual straining stage. Selected areas of the film surface were imaged at zero strain and at global strains of 1.4%, 3.2%, 4.5%, 6.7%, and 8.5%. For each straining step the SEM chamber was vented and the screw-driven movable arm of the straining stage was displaced manually. Usage of a manual tensile stage allows to avoid potential artefacts in SEM images, enabling fast and precise image correlation. The global strain values were measured directly in SEM by measuring the distance between two markers at low magnification. At each loading step, five areas were imaged at a magnification of 15,000x (field of view equals 20 μm) and resolution of 1024 × 768 pixels with an acceleration voltage of 3 kV. These images were analyzed using a free version of GOM Correlate DIC software to construct the maps of local strain. Since the sample surfaces exhibit natural random porosity, no additional speckle pattern was required for DIC.

To extract linear crack densities and crack lengths, the DIC strain maps at maximum strain (8.5%) were utilized. For linear crack density, straight lines parallel to the straining direction are drawn across each image and the number of intersects is divided by the length of the line. Altogether 25 linear crack density measurements were performed, five per imaged area. The crack lengths were measured as a projection of the crack length onto the direction perpendicular to the straining direction.

3. Results and discussion

3.1. Optical and electrical properties

Optical characterization of the printed layers was carried out by recording UV-VIS spectra of the two film types. The ultrathin films exhibit high transparency with transmittance increasing from 82% at the wavelength of 800 nm to 92% at the wavelength of 400 nm. For the 150 nm thick film, blockage of all light across the visible spectrum was observed, with a transmittance of < 1 %. The measured spectra are provided in the supplementary material as Fig. S1.

Optical and electrical properties of as-deposited films are summarized in Table 1 along with the parameters of an ITO coating from our previous work [47]. In order to quantitatively compare different electrode materials, we employ Haacke's figure of merit (FOM), in which the optical transmission T is related to the sheet resistance R_s by FOM $= T^{10}$ R_s^{-1} [48]. Although more complex concepts of FOM have been introduced recently (see, e.g. [49]), we have used the original Haacke FOM for the sake of comparability. The transparent electrode obtained from the MOD ink has a value of FOM only slightly lower than ITO, thus indicating a favorable combination of optical transparency and electrical conductivity. The resistivity values were obtained using the measured sheet resistance and nominal film thickness obtained from gravimetric measurements, i.e. not considering the presence of pores or discontinuities which are discussed later on. Nevertheless, the effective resistivity of the transparent film is significantly lower than that of ITO, although being about 50 times larger in comparison to bulk silver. The low-resistance coating with a nominal thickness of 150 nm has an effective resistivity only 7.5 times larger than bulk silver, proving its suitability to be used as a regular, non-transparent conductor in flexible electronics. Therefore, by appropriately adjusting the printing-curing process, electrodes with different optoelectronic properties can be produced.

3.2. Morphology and structure

The ultrathin transparent films exhibit a complex microstructure containing areas with different morphology, as shown in the SEM analysis depicted in Fig. 1. Dendritic growth during the solidification process leads to characteristic snowflake-like patterns of silver separated by voids that appear black in the SEM images (Figs. 1a and 1b). An example of a presumed nucleation point of dendritic solidification is demonstrated in Fig. 1a with arrows depicting the growth directions. The pores (or voids) in the film can be classified into two groups according to their geometry and origin, as shown in Fig. 1b and the corresponding inset. The first type includes the nano-sized pores with diameters below 50 nm, which are formed within the solidified areas. They appear presumably due to the decrease in volume during the curing process. The pores of the second type are located between the dendritic arms and can be significantly larger, up to a few micrometers in size, although they typically have dimensions in the sub-micrometer range. In addition to this dendritic microstructure, ultrathin films contain areas characterized by a homogeneous percolated network of nano-sized (20-50 nm) crystallites separated by pores of approximately the same size, as depicted in Fig. 1c. On the macroscopic scale, the homogeneous percolated network topology is dominant within the film and covers about 60 % of the total area. As can be seen in a low-magnification SEM image shown in Fig. 1d, the dendritic colonies with sizes up to a mm are randomly distributed within this matrix.

The porosity (i.e., surface fraction occupied by pores) determined by grayscale thresholding is about 30% on average, specifically 28%, 31%, and 33% for the images shown in Figs. 1a; 1b, and 1c, respectively. For transparent conductors based on intrinsically non-transparent materials, such as silver, some porosity is required to grant acceptable values of optical transmission. However, large porosity values would inevitably deteriorate the effective conductivity of the film. Both dendritic and homogeneous morphologies can result in a favorable combination of optical transparency and electrical conductivity required for transparent electrode applications, assuming good interconnectivity of dendritic arms or nanosized ligaments.

Table 1
Electrical and optical properties of the conductive layers considered in this work.

Sample	Ink	Nominal thickness, nm	Sheet resistance, Ω sq^{-1}	Effective resistivity, μΩ*cm	Effective conductivity[b], S cm^{-1} (% bulk)	Transmittance[c], %	FOM, $Ω^{-1}$
transparent	OTech T1053	30[a]	26.0	78	1.28 × 10^4 (2.08)	86.1	8.61 × 10^{-3}
low-resistance	OTech Jet 1151	150[a]	0.8	12	8.33 × 10^4 (13.23)	0.7	3.53 × 10^{-22}
ITO	-	120	15.0	180	-	84.0	11.60 × 10^{-3}

a) according to gravimetric measurements
b) considering tabulated conductivity value for metallic Ag of 6.3 × 10^5 S cm^{-1}
c) at 550 nm

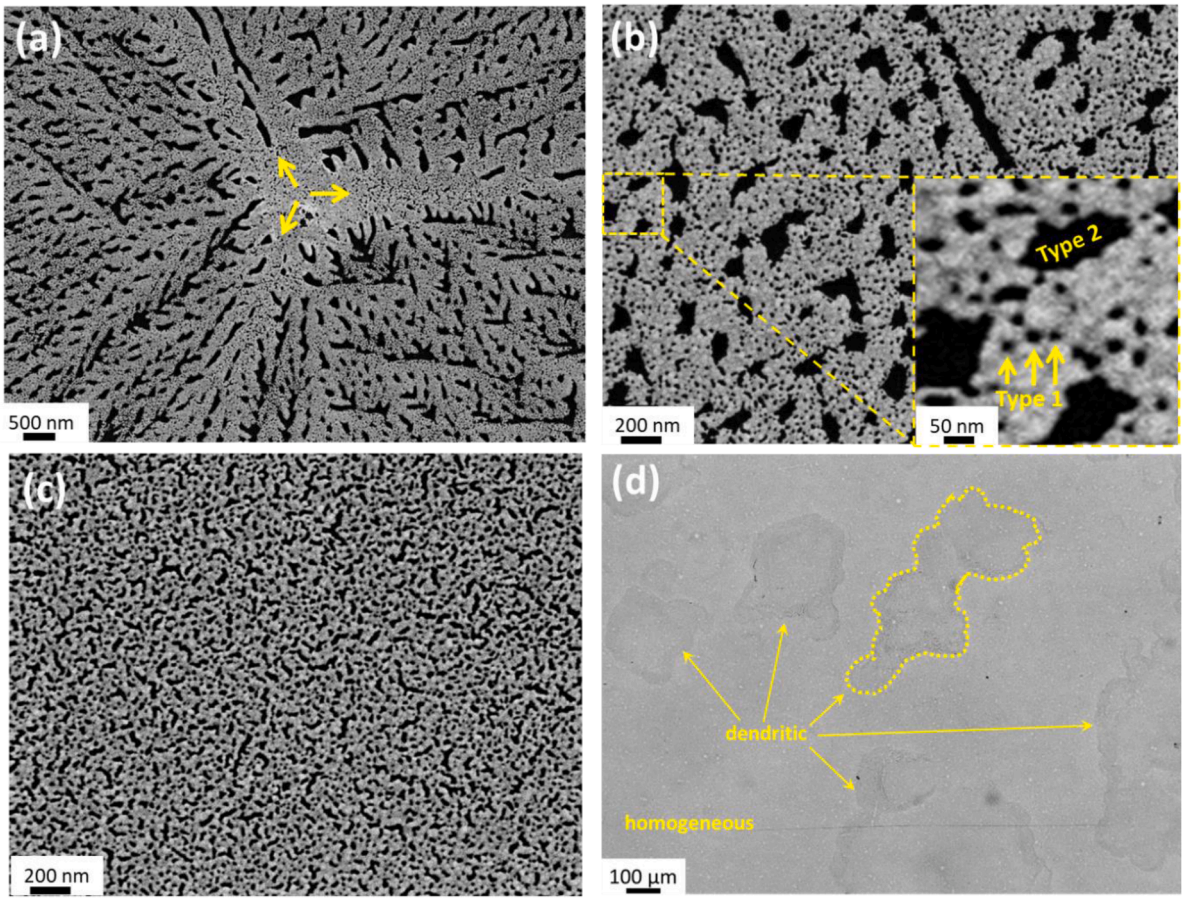

Fig. 1. SEM characterization of nanoporous transparent conductive films. (a): center of a dendritic colony with arrows showing the dendrite growth direction from a presumed nucleation point. (b): typical microstructure of a dendritic colony with the inset showing a corresponding enlarged view and two types of pores. (c): an example of a homogeneous percolated network topology. (d): low-magnification SEM image demonstrating macroscopic distribution of dendritic colonies.

It is worth noting that the morphology presented in Fig. 1c is very similar to the gold nanomesh electrodes obtained by vapor de-alloying process of ultrathin Au-Cu alloy films [20] or to the nanoporous metal films obtained by plasma-assisted dry synthesis process [23]. However, in contrast to these rather complex, multi-step processes, the transparent electrode shown in Fig. 1 was obtained through a single printing-curing step and results in a lower sheet resistance and a higher optical transparency [20,23].

The structure of thicker, non-transparent but low-resistance films can be characterized as a network of interconnected silver particles with homogeneously distributed pores in between, as shown in Fig. 2. The characteristic sizes of the particles lie between 50 and 200 nm as depicted by the dotted contours in Fig. 2b. The surface porosity is about 9% and varies only slightly throughout the film. In contrast to ultrathin films, where porosity is required for high optical transmission, regular conductors should have a dense structure to maximize the effective conductivity. Therefore, further process optimization is required to obtain denser films which could serve as regular metallization layers in a

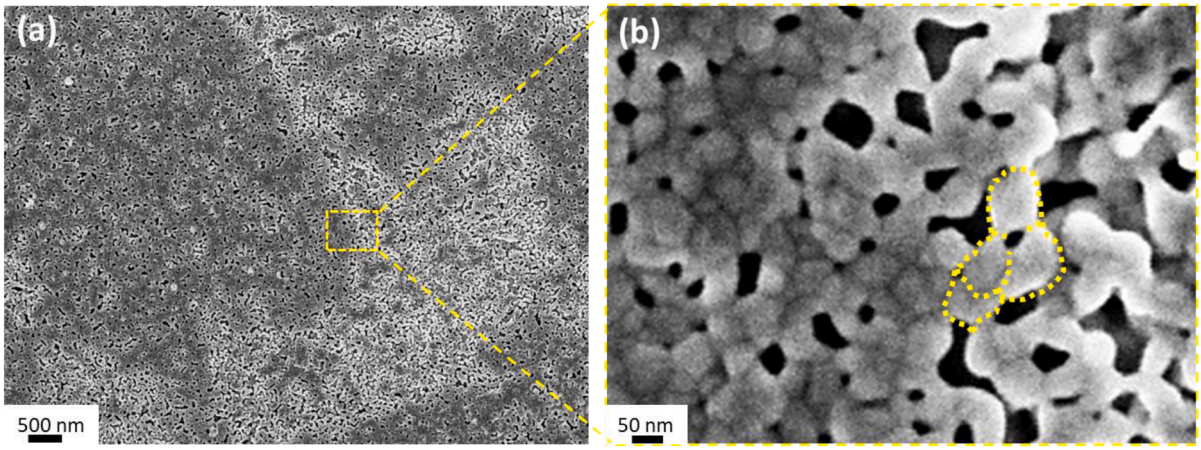

Fig. 2. SEM characterization of the low-resistance films. Typical surface topology is given in (a) with the enlarged view from the corresponding marked area shown in (b). The yellow dotted contours mark a characteristic ligament consisting of four particles.

future device.

3.3. Mechanical properties and fracture behavior

In addition to appropriate optoelectronic properties, thin film electrodes deposited on flexible substrates need to be mechanically stable. Tensile tests with in-situ resistance measurements were performed using a standard approach described elsewhere [50,51]. To enable direct comparison of different films, the recorded resistance R during straining is normalized to the initial resistance of the same sample R_0. Recorded in-situ resistance is typically considered with respect to the theoretical constant volume approximation curve, showing predicted resistance change in case of perfect plastic deformation, i.e. when no cracks are induced [50,51]. As can be seen in Fig. 3, the resistance of both ultrathin transparent ink and low-resistance inks starts to deviate from the crack-free deformation curve at the strain of about 0.5%, which is an indicator of crack formation. However, the resistance growth with increasing strain is moderate, so that both films stay conductive at 10% strain, only losing approximately half of the initial conductivity. Moderate loss of conductivity with increasing strain typically implies that induced cracks are short and not well interconnected with each other [52].

For comparison, the electro-mechanical behavior of ink-jet printed silver from nanoparticle (NP)-based inks with a thickness of 800 nm on PET from [43] is also shown in Fig. 3 along with the behavior of a commercial ITO coating on PET. Although the NP-based film exhibits a larger crack-free deformation range of about 1.5%, the resistance grows much faster at higher strain values, indicating more severe cracking of the conductive material. The ITO coating is intrinsically brittle, therefore recorded resistance grows rapidly after reaching the elastic limit of about 1%, indicating catastrophic mechanical and electrical failure.

The observed crack onset strain of 0.5% in the nanoporous films is surprising since in continuous films first cracks are formed first after reaching the elastic limit which is typically between 1% and 2% strain [43,53], even in the case of brittle ITO [54,55]. To explain this phenomenon, we hypothesize that in stochastically formed nanoporous films, some ligaments are particularly weakly bonded and begin to break at strain levels lower than the material's elastic limit.

To characterize the morphology of the damage after the applied strain of 10%, post-mortem SEM characterization was performed. However, due to the porous surface and viscoelastic substrate relaxation, which exposes compressive stress on the film after unloading, unambiguous detection of the induced damage was not possible, see supplementary Fig. S2 for more details. In order to capture the nanoscale mechanisms of deformation and fracture in considered systems, a series of in-situ straining experiments in SEM with DIC analysis was conducted.

In-situ SEM images of the low-resistance coating after applied strains of 1.4%, 3.2%, and 6.4% overlapped with the strain maps obtained from DIC analysis are shown in Figs. 4a; 4b; and 4c, respectively. The corresponding enlarged images are given in Figs. 4d; 4e; and 4f, respectively. The color map represents Mises strain which accounts for all components (ε_{xx}, ε_{yy}, ε_{xy}) of the 2D deviatoric strain tensor. Mises strain reflects the amount of local distortion energy density during mechanical loading. Already after the first loading step with the applied global strain of 1.4%, the distribution of local strains is highly inhomogeneous. In Fig. 4d a region of high local strain of about 6% is depicted by the white dotted curve. After the second loading step, corresponding to a total global strain of 3.2%, the local Mises strain exceeds 20% within the strain localization areas (Figs. 4b and 4e). At the applied strain of 6.4%, the local strain distributions consist of interchanging areas of high and low strains (Figs. 4c and 4d).

To provide a more quantitative description of strain evolution, the average major strain component (ε_{yy}) from the areas depicted as "A" and "B" in Fig. 4d, along with the average values from the whole area, are shown in Fig. 5. The average strain from area "A" reaches high values of over 40%, whereas within the neighboring area "B" it stays below 0.5% (see the inset in Fig. 5). It is important to note that the strain calculation in DIC analysis is based on the total surface displacements showing the sum of elastic strain, plastic strain, and displacement due to the crack opening after local rupture. Although the unambiguous separation of these three contributions is not possible directly, the high-strain regions can be identified as cracks due to the following two reasons. Firstly, extended plasticity with a plastic strain of over 20% is not expected for the nanocrystalline ligaments due to suppression of dislocation-based plasticity, also known as the Hall-Petch effect [56]. Secondly, the appearance of virtually fully relaxed zones, such as area "B", is a typical consequence of strain relaxation on the crack edges, as described by the shear lag model [57].

The ultrathin films analyzed using SEM-DIC revealed qualitatively similar morphology of local strain distribution, shown in supplementary Fig. S3. However, since the films are ultra-thin, non-continuous, and on a non-conductive substrate, the static charging of the substrate and consequential image drift made quantitative interpretation of the DIC

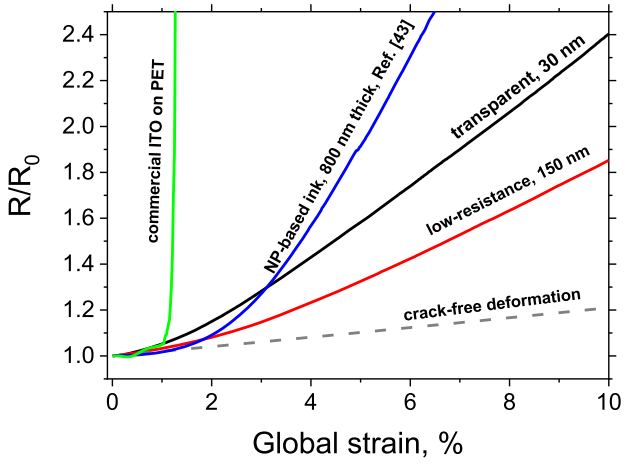

Fig. 3. *Dependence of the relative resistance, recorded in-situ during straining, on the applied strain. Along with the low-resistance and transparent samples considered in this work, the behavior of printed silver based on NP ink from [43], commercial ITO on PET, as well as the theoretical prediction for crack-free deformation are shown for comparison.*

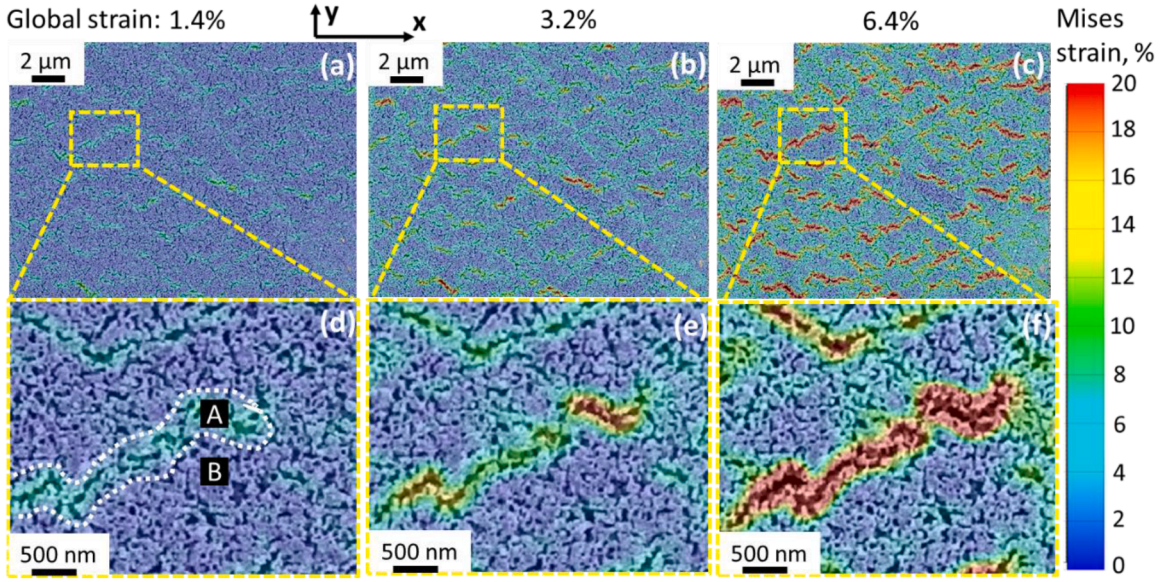

Fig. 4. SEM-DIC analysis of deformation and fracture behavior of the low-resistance sample. The SEM images are overlaid with the distributions of local Mises strain employing the color scale given on the right. The same surface area is shown in (a, b, c) after the applied global strain of 1.4%, 3.2%, and 6.4%, respectively. Enlarged views from the areas marked by yellow rectangles are shown in (d, e, f), respectively. The white dotted contour in (d) shows an example of local strain concentration. The black squares marked with "A" and "B" in (d) depict the areas used for calculations of average strain values shown in Fig. 5. The straining direction is vertical.

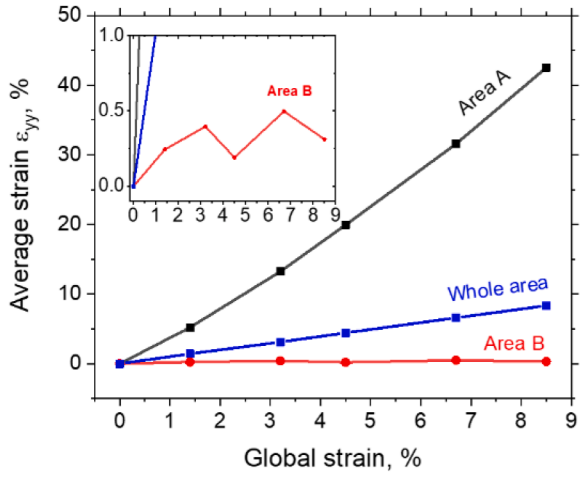

Fig. 5. The evolution of the average major strain component (ε_{yy}) value obtained from the areas marked by "A" and "B" and from the whole area analyzed by DIC in Fig. 4. The curves are correspondingly marked directly on the plot. The inset shows the enlarged view for the strains below 1%.

analysis difficult [58].

The results of the DIC analysis agree very well with the in-situ resistance measurements, thereby establishing a complete picture of deformation and fracture processes during tensile loading. Rupture of single ligaments starts at low global strains of about 0.5%, leading to the appearance of nanocracks and, consequently, the growth of resistance beyond the constant volume approximation (Fig. 3). With increasing applied strain, further ligaments rupture, leading to crack growth and resistance increase, however, the cracks have zig-zag morphology and lengths which do not exceed 3-4 μm (Fig. 4c). Moreover, the cracks are homogeneously distributed throughout the film and do not form an interconnected network, leading to rather moderate resistance growth after 10% of applied global strain (Fig. 3). In fact, such a crack pattern mimics the famous "kirigami approach" which utilizes intentional introduction of stress concentrating defects to achieve a significant extension of the stretchability of the whole composite structure [59]. Crack patterns consisting of homogeneously distributed, short, and isolated cracks are advantageous from the point of view of electrical stability. Indeed, despite the relatively high crack density, numerous conductive paths for electric current flow are retained.

A quantitative relationship connecting electrical degradation with crack pattern parameters proposed in [52] states that the relative resistance (R/R_0) can be estimated as

$$\frac{R}{R_0} = 1 + \frac{1}{\sqrt{2}} C_l l_0 + \frac{1}{2} C_l^2 l_0^2, \quad (1)$$

where C_l is the linear crack density (number of cracks per length in the direction of electric current flow) and l_0 is the average crack length in the direction perpendicular to the current flow. Based on DIC analysis of five areas with the dimensions of approximately 15 × 25 μm^2 each, the experimental crack density of (0.48±0.08) μm^{-1} and the average crack length and corresponding standard deviation of (1.7±1.0) μm were measured. The high value of the standard deviation reflects very broad distribution of the crack lengths. By substituting the measured mean values into Eq. (1), the resistance growth value of R/R_0=1.92 is estimated. This value corresponds well to the experimental resistance growth at 10% strain shown in Fig. 3 (R/R_0=1.82) confirming that the quantitative correlation between the electrical degradation and crack pattern parameters is adequately described by Eq. (1). Therefore, Eq. (1) can be utilized to estimate the crack pattern parameters on the basis of electrical resistance growth, avoiding time-consuming in-situ SEM analysis.

The combination of in-situ resistance measurements, in-situ SEM-DIC analysis, and the empirical relation between electrical degradation and crack development provides a full picture of the deformation behavior and electro-mechanical stability of the printed electrodes.

3.4. Cyclic reliability

From the point of view of flexible electronics applications, a flexible device should sustain rather small mechanical strains but repeatedly, over many loading cycles without electrical degradation. It was shown that conductors which exhibit good performance during monotonic loading, such as pure ductile metals (like Cu, Ag or Au) fabricated by physical vapor deposition, might quickly accumulate damage during

cyclic loading with subsequent mechanical and electrical degradation [60,61]. The evolution of electrical resistance during cyclic loading with the cyclic strain of 1% and 2% is depicted in Fig. 6 for both transparent and low-resistance samples.

Substantial resistance increase is observed in low-resistance samples subjected to 2% cyclic strain (Fig. 6a) while the transparent samples exhibit very good performance during 10,000 cycles. In the enlarged view of the first 10 cycles (Fig. 6b) the fine structure of the recorded signal allows to resolve each applied straining cycle with resistance reaching maxima at maximal applied strain and minima at zero strain. The observed evolution of in-situ resistance corresponds very well to the analysis of the monotonic behavior. The critical strain to initiate cracks during the monotonic tensile test (Fig. 3) was about 0.5% for both transparent and low-resistance samples. Therefore, the cracks should be initiated already during the first cycle, which is indeed observed in Fig. 6b, since the resistance does not return to the initial value after the first cycle. This observation confirms the suggestion that some ligaments are particularly weakly bonded with each other and break at such a low strain. However, after the weakest ligaments are broken during a few initial cycles, no significant crack propagation is observed in *transparent* samples. This follows from the fact that the resistance growth saturates quickly and the overall resistance growth after 10,000 cycles is about 20% for the cyclic strain of 1% and about 30% for the cyclic strain of 2%. The fine structure of the resistance signal after 9500 cycles is provided in supplementary figure Fig. S4. It is worth noting that the tensile strain of 2% corresponds to a bending radius of only 2.5 mm for a substrate thickness of 100 μm as follows from the estimative relation $\varepsilon=t/2R$, where ε is the surface strain, t is the substrate thickness and R is the bending radius. Therefore, the ultrathin transparent layers should demonstrate very good stability during repeated bending.

In low-resistance samples, the cyclic strain of 2% indeed leads to crack growth with increasing number of cycles which is manifested by continuous growth of average resistance. An attempt to describe the morphology of the cracks induced by cyclic loading and compare it to the crack morphology during monotonic loading (Fig. 4) was performed, however, in post-mortem images it was not possible to unambiguously identify the cracks. Substrate viscoelasticity imposes compressive stress on the film upon unloading [62] leading to the crack re-bridging effect [63]. Although in the case of continuous sputter-deposited films the cracks can still be clearly identified by propagating surface deformations and extrusions [63], in nanoporous film it is not possible due to the absence of extrusions and strong variations in image contrast caused by the pores. Low-resistance samples subjected to 1% of cyclic strain show good reliability with overall resistance growth of 30% after 10,000 cycles.

To benchmark the combined electrical, optical, and mechanical performance of our ultrathin transparent electrode against other ITO-free alternatives, we focus on silver nanowire (AgNW)-based electrodes which are discussed in detail in two recent reviews [64,65]. Our nanoporous electrode exhibits an optical transparency of 86% and a sheet resistance of 26 Ω sq^{-1}, which are comparable to the best-performing AgNW electrodes and their hybrid forms with graphene, carbon nanotubes, or PEDOT:PSS [64]. Notably, our electrode demonstrates superior mechanical robustness: while typical AgNW-based systems withstand bending radii between 5 and 30 mm [64], our electrode maintains performance at an equivalent bending radius of just 2.5 mm.

Given the additional advantages of MOD inks over nanowire-based inks discussed in the introduction, such as simplified processing, enhanced shelf life, and lower material consumption, our nanoporous electrodes represent a promising technology for next-generation transparent conductive coatings.

4. Summary and conclusions

In this work, we focused on the establishment of the structure-property relationships connecting nano- and mesoscale morphology with macroscopic mechanical behavior and electrical performance of ultrathin transparent conductive layers based on plasma-sintered silver MOD inks. In addition, low-resistance opaque electrodes were fabricated using the same process and analyzed for the sake of comparison.

Both transparent and low-resistance films exhibit naturally occurring nanoporous microstructure. Transparent films consist of 2D percolated network of silver ligaments (either homogeneous or in the form of dendritic colonies) with porosity of about 30%, leading to a favorable combination of optical transparency (over 80%) and sheet resistance (26 Ω sq^{-1}). The low-resistance films have surface porosity of about 9% and typical ligament sizes of about 100 nm resulting in sheet resistance of 0.8 Ω sq^{-1}.

When subjected to tensile mechanical load, the resistance of both ultrathin and thicker low-resistance films start to grow when reaching the strain values of about 0.5%. Such a low value can be explained by the existence of numerous “weak links”, i.e. ligaments which are loosely connected with each other after the curing process and rupture readily during stretching. At the same time, as confirmed by in-situ SEM-DIC analysis, random distribution of such weak ligaments leads to the homogeneous generation of nanocracks and zig-zag crack propagation when higher strain (up to 10%) is applied. As a result, the cracks mutually hinder propagation of each other, providing a basis for extended stretchability and preventing the appearance of catastrophic cracking and significant deterioration of electrical conductivity. Ultrathin transparent layers demonstrate exceptional stability during cyclic

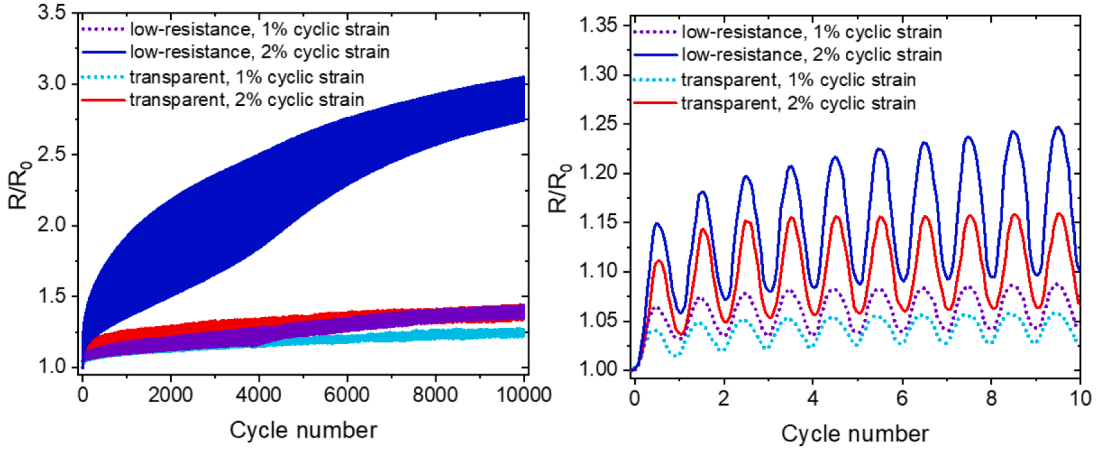

Fig. 6. Evolution of electrical resistance during cyclic loading. The overview for 10,000 cycles is shown in (a); enlarged view demonstrating the fine structure of the resistance signal for the first 10 cycles is depicted in (b). Both low-resistance and transparent samples were tested at cyclic strains of 1% and 2% (see legend).

loading conditions. Although marginal resistance growth occurs during the initial few cycles, even the cyclic strain of 2% does not induce a significant electrical degradation after 10,000 cycles. At the same time, the nanoporosity of the electrode might require additional specially designed reliability tests to prove, for example, resistance against mechanical wear or stability against local delamination of the ligaments.

In general, better understanding of the relationships between the film morphology and film performance (in terms of optical transparency, conductivity, and mechanical stability) is required to enable knowledge-based optimization routines for single-layer ultrathin transparent electrodes based on MOD inks.

Availability of data and material

Collected data can be provided by the authors upon a reasonable request.

CRediT authorship contribution statement

Oleksandr Glushko: Writing – review & editing, Writing – original draft, Visualization, Methodology, Investigation, Formal analysis, Conceptualization. **Michael Hengge:** Investigation, Data curation. **Konstantin Livanov:** Writing – review & editing, Writing – original draft, Visualization, Investigation, Conceptualization. **Natalia Zamoshchik:** Writing – review & editing, Conceptualization. **Emil J.W. List-Kratochvil:** Resources, Writing – review & editing, Funding acquisition. **Felix Hermerschmidt:** Conceptualization, Validation, Investigation, Writing – original draft, Writing – review & editing, Visualization.

Declaration of competing interest

The authors declare that they have no known competing financial interests or personal relationships that could have appeared to influence the work reported in this paper.

Acknowledgements

OG would like to acknowledge full financial support from the Austrian Science Fund (FWF), Project No. P31544-NBL. This work was conducted in the framework of the Joint Lab GEN_FAB. The authors thank Professor N. Koch for granting access to laboratory infrastructure.

Supplementary materials

Supplementary material associated with this article can be found, in the online version, at doi:10.1016/j.mtla.2025.102483.

References

[1] Z. Zhao, K. Liu, Y. Liu, Y. Guo, Y. Liu, Intrinsically flexible displays: key materials and devices, Natl. Sci. Rev. 9 (2022), https://doi.org/10.1093/nsr/nwac090.
[2] Y.-F. Liu, J. Feng, Y.-G. Bi, D. Yin, H.-B. Sun, Recent developments in flexible organic light-emitting devices, Adv. Mater. Technol. 4 (2019) 1800371, https://doi.org/10.1002/admt.201800371.
[3] A.H. Anwer, N. Khan, M.Z. Ansari, S.-S. Baek, H. Yi, S. Kim, S.M. Noh, C. Jeong, Recent advances in touch sensors for flexible wearable devices, Sensors 22 (2022) 4460, https://doi.org/10.3390/s22124460.
[4] S.D. Lawaniya, S. Kumar, Y. Yu, H.G. Rubahn, Y.K. Mishra, K. Awasthi, Functional nanomaterials in flexible gas sensors: recent progress and future prospects, Mater. Today Chem. 29 (2023) 101428, https://doi.org/10.1016/j.mtchem.2023.101428.
[5] F. Gao, C. Liu, L. Zhang, T. Liu, Z. Wang, Z. Song, H. Cai, Z. Fang, J. Chen, J. Wang, M. Han, J. Wang, K. Lin, R. Wang, M. Li, Q. Mei, X. Ma, S. Liang, G. Gou, N. Xue, Wearable and flexible electrochemical sensors for sweat analysis: a review, Microsyst. Nanoeng. 9 (2023) 1–21, https://doi.org/10.1038/s41378-022-00443-6.
[6] S. Kim, H. Van Quy, C.W. Bark, Photovoltaic technologies for flexible solar cells: beyond silicon, Mater. Today Energy 19 (2021) 100583, https://doi.org/10.1016/j.mtener.2020.100583.
[7] H. Kim, C.M. Gilmore, A. Piqué, J.S. Horwitz, H. Mattoussi, H. Murata, Z.H. Kafafi, D.B. Chrisey, Electrical, optical, and structural properties of indium–tin–oxide thin films for organic light-emitting devices, J. Appl. Phys. 86 (1999) 6451–6461, https://doi.org/10.1063/1.371708.
[8] C. Peng, Z. Jia, D. Bianculli, T. Li, J. Lou, In situ electro-mechanical experiments and mechanics modeling of tensile cracking in indium tin oxide thin films on polyimide substrates, J. Appl. Phys. 109 (2011) 1–8, https://doi.org/10.1063/1.3592341.
[9] European Commission, Critical raw materials resilience: charting a path towards greater security and sustainability, COM (2020), 2020, https://eur-lex.europa.eu/legal-content/EN/TXT/PDF/?uri=CELEX:52020DC0474&from=DE.
[10] S. Kim, J.-L. Lee, Design of dielectric/metal/dielectric transparent electrodes for flexible electronics, J. Photon. Energy 2 (2012) 021215, https://doi.org/10.1117/1.JPE.2.021215.
[11] V.H. Nguyen, D.T. Papanastasiou, J. Resende, L. Bardet, T. Sannicolo, C. Jiménez, D. Muñoz-Rojas, N.D. Nguyen, D. Bellet, Advances in flexible metallic transparent electrodes, Small 18 (2022), https://doi.org/10.1002/smll.202106006.
[12] L. Kinner, M. Bauch, R.A. Wibowo, G. Ligorio, E.J.W. List-Kratochvil, T. Dimopoulos, Polymer interlayers on flexible PET substrates enabling ultra-high performance, ITO-free dielectric/metal/dielectric transparent electrode, Mater. Des. 168 (2019) 107663, https://doi.org/10.1016/j.matdes.2019.107663.
[13] W.K. Kim, S. Lee, D. Hee Lee, I. Hee Park, J. Seong Bae, T. Woo Lee, J.Y. Kim, J. Hun Park, Y. Chan Cho, C. Ryong Cho, S.Y. Jeong, Cu mesh for flexible transparent conductive electrodes, Sci. Rep. 5 (2015) 1–8, https://doi.org/10.1038/srep10715.
[14] A. Khan, S. Lee, T. Jang, Z. Xiong, C. Zhang, J. Tang, L.J. Guo, L. Wen-Di, High-performance flexible transparent electrode with an embedded metal mesh fabricated by cost-effective solution process, Small 12 (2016) 3021–3030, https://doi.org/10.1002/smll.201600309.
[15] H.B. Lee, W.Y. Jin, M.M. Ovhal, N. Kumar, J.W. Kang, Flexible transparent conducting electrodes based on metal meshes for organic optoelectronic device applications: a review, J. Mater. Chem. C 7 (2019) 1087–1110, https://doi.org/10.1039/c8tc04423f.
[16] T. Sannicolo, M. Lagrange, A. Cabos, C. Celle, J.P. Simonato, D. Bellet, Metallic nanowire-based transparent electrodes for next generation flexible devices: a review, Small 12 (2016) 6052–6075, https://doi.org/10.1002/smll.201602581.
[17] W. Li, H. Zhang, S. Shi, J. Xu, X. Qin, Q. He, K. Yang, W. Dai, G. Liu, Q. Zhou, H. Yu, S.R.P. Silva, M. Fahlman, Recent progress in silver nanowire networks for flexible organic electronics, J. Mater. Chem. C 8 (2020) 4636–4674, https://doi.org/10.1039/c9tc06865a.
[18] M. Vaseem, G. McKerricher, A. Shamim, Robust design of a particle-free silver-organo-complex ink with high conductivity and inkjet stability for flexible electronics, ACS Appl. Mater. Interfaces 8 (2016) 177–186, https://doi.org/10.1021/acsami.5b08125.
[19] L. Kinner, F. Hermerschmidt, T. Dimopoulos, E.J.W. List-Kratochvil, Implementation of flexible embedded nanowire electrodes in organic light-emitting diodes, Phys. Status Solidi - Rapid Res. Lett. 14 (2020) 1–6, https://doi.org/10.1002/pssr.202000305.
[20] A. Chauvin, W. Txia Cha Heu, J. Buh, P.Y. Tessier, A.A. El Mel, Vapor dealloying of ultra-thin films: a promising concept for the fabrication of highly flexible transparent conductive metal nanomesh electrodes, Npj Flex. Electron. 3 (2019) 1–6, https://doi.org/10.1038/s41528-019-0049-1.
[21] Y. Zhang, X. Guo, J. Huang, Z. Ren, H. Hu, P. Li, X. Lu, Z. Wu, T. Xiao, Y. Zhu, G. Li, Z. Zheng, Solution process formation of high performance, stable nanostructured transparent metal electrodes via displacement-diffusion-etch process, Npj Flex. Electron. 6 (2022) 4, https://doi.org/10.1038/s41528-022-00134-2.
[22] W. Yang, F. Hermerschmidt, F. Mathies, E.J.W. List-Kratochvil, Comparing low-temperature thermal and plasma sintering processes of a tailored silver particle-free ink, J. Mater. Sci. Mater. Electron. 32 (2021) 6312–6322, https://doi.org/10.1007/s10854-021-05347-1.
[23] H. Kwon, H.N. Barad, A.R. Silva Olaya, M. Alarcón-Correa, K. Hahn, G. Richter, G. Wittstock, P. Fischer, Dry synthesis of pure and ultrathin nanoporous metallic films, ACS Appl. Mater. Interfaces 15 (2023) 5620–5627, https://doi.org/10.1021/acsami.2c19584.
[24] D. Li, W.Y. Lai, Y.Z. Zhang, W. Huang, Printable transparent conductive films for flexible electronics, Adv. Mater. 30 (2018) 1–24, https://doi.org/10.1002/adma.201704738.
[25] B. Zhang, R. Gong, Y. Zhang, Y. Li, L. Zhu, Recent progress in dielectric/metal/dielectric electrodes for foldable light-emitting devices, Nanotechnol. Rev. 12 (2023) 1–24, https://doi.org/10.1515/ntrev-2023-0578.
[26] L. Meng, W. Wang, B. Xu, J. Qin, K. Zhang, H. Liu, Solution-processed flexible transparent electrodes for printable electronics, ACS Nano 17 (2023) 4180–4192, https://doi.org/10.1021/acsnano.2c10999.
[27] Y. Choi, K. Seong, Y. Piao, Metal−organic decomposition ink for printed electronics, Adv. Mater. Interfaces 6 (2019) 1901002, https://doi.org/10.1002/admi.201901002.
[28] S.P. Douglas, S. Mrig, C.E. Knapp, MODs vs. NPs: vying for the future of printed electronics, Chem. – Eur. J 27 (2021) 8062–8081, https://doi.org/10.1002/chem.202004860.
[29] W. Yang, E.J.W. List-Kratochvil, C. Wang, Metal particle-free inks for printed flexible electronics, J. Mater. Chem. C 7 (2019) 15098–15117, https://doi.org/10.1039/C9TC05463D.
[30] A.J. Kell, K. Wagner, X. Liu, B.H. Lessard, C. Paquet, Advanced applications of metal–organic decomposition inks in printed electronics, ACS Appl. Electron. Mater. (2023), https://doi.org/10.1021/acsaelm.3c00910.
[31] Y. Farraj, M. Grouchko, S. Magdassi, Self-reduction of a copper complex MOD ink for inkjet printing conductive patterns on plastics, Chem. Commun. 51 (2015) 1587–1590, https://doi.org/10.1039/C4CC08749F.

[32] C. Schoner, A. Tuchscherer, T. Blaudeck, S.F. Jahn, R.R. Baumann, H. Lang, Particle-free gold metal–organic decomposition ink for inkjet printing of gold structures, Thin Solid Films 531 (2013) 147–151, https://doi.org/10.1016/j.tsf.2013.01.027.
[33] H.M. Lee, H.B. Lee, D.S. Jung, J.-Y. Yun, S.H. Ko, S.Bin Park, Solution processed aluminum paper for flexible electronics, Langmuir 28 (2012) 13127–13135, https://doi.org/10.1021/la302479x.
[34] Y. Farraj, A. Smooha, A. Kamyshny, S. Magdassi, Plasma-induced decomposition of copper complex ink for the formation of highly conductive copper tracks on heat-sensitive substrates, ACS Appl. Mater. Interfaces 9 (2017) 8766–8773, https://doi.org/10.1021/acsami.6b14462.
[35] W. Li, M. Xu, J. Gao, X. Zhang, H. Huang, R. Zhao, X. Zhu, Y. Yang, L. Luo, M. Chen, H. Ji, L. Zheng, X. Wang, W. Huang, Large-scale ultra-robust MoS2 patterns directly synthesized on polymer substrate for flexible sensing electronics, Adv. Mater. 35 (2023) 1–13, https://doi.org/10.1002/adma.202207447.
[36] S. Svanström, T.J. Jacobsson, G. Boschloo, E.M.J. Johansson, H. Rensmo, U. B. Cappel, Degradation mechanism of silver metal deposited on lead halide perovskites, ACS Appl. Mater. Interfaces 12 (2020) 7212–7221, https://doi.org/10.1021/acsami.9b20315.
[37] F. Hermerschmidt, D. Burmeister, G. Ligorio, S.M. Pozov, R. Ward, S.A. Choulis, E. J.W. List-Kratochvil, Truly low temperature sintering of printed copper ink using formic acid, Adv. Mater. Technol. 3 (2018) 1–6, https://doi.org/10.1002/admt.201800146.
[38] W. Yang, F. Mathies, E.L. Unger, F. Hermerschmidt, E.J.W. List-Kratochvil, One-pot synthesis of a stable and cost-effective silver particle-free ink for inkjet-printed flexible electronics, J. Mater. Chem. C 8 (2020) 16443–16451, https://doi.org/10.1039/d0tc03864d.
[39] A.J. Kell, K. Wagner, X. Liu, H. Lessard, C. Paquet, Advanced applications of metal − organic decomposition inks in printed electronics, (2023). https://doi.org/10.1021/acsaelm.3c00910.
[40] M. Hengge, K. Livanov, N. Zamoshchik, F. Hermerschmidt, E.J.W. List-Kratochvil, ITO-free OLEDs utilizing inkjet-printed and low temperature plasma-sintered Ag electrodes, Flex. Print. Electron. 6 (2021) 015009, https://doi.org/10.1088/2058-8585/abe604.
[41] N. Lu, X. Wang, Z. Suo, J. Vlassak, Metal films on polymer substrates stretched beyond 50%, Appl. Phys. Lett. 91 (2007) 1–4, https://doi.org/10.1063/1.2817234.
[42] G.D. Sim, Y. Hwangbo, H.H. Kim, S.B. Lee, J.J. Vlassak, Fatigue of polymer-supported Ag thin films, Scr. Mater. 66 (2012) 915–918, https://doi.org/10.1016/j.scriptamat.2012.02.030.
[43] O. Glushko, A. Klug, E.J.W.W. List-Kratochvil, M.J. Cordill, Monotonic and cyclic mechanical reliability of metallization lines on polymer substrates, J. Mater. Res. 32 (2017) 1760–1769, https://doi.org/10.1557/jmr.2017.121.
[44] Y. Zamoshchik, N, K. Livanov, Sheynin, method for metal layer formation. https://patents.google.com/patent/US20200017974A1, 2020.
[45] S. Dou, L. Tao, R. Wang, S. El Hankari, R. Chen, S. Wang, Plasma-assisted synthesis and surface modification of electrode materials for renewable energy, Adv. Mater. 30 (2018) 1705850, https://doi.org/10.1002/adma.201705850.
[46] J. Zheng, B. Sun, R. Yang, X. Song, X. Li, Y. Pu, Metal Al produced by H 2 plasma reduction of AlCl 3 : a thermodynamic and kinetic study on the plasma chemistry, J. Phys. Chem. B 112 (2008) 12748–12752, https://doi.org/10.1021/jp8035204.
[47] L. Kinner, T. Dimopoulos, G. Ligorio, E.J.W. List-Kratochvil, F. Hermerschmidt, High performance organic light-emitting diodes employing ITO-free and flexible TiO x /Ag/Al:zno electrodes, RSC Adv. 11 (2021) 17324–17331, https://doi.org/10.1039/D1RA02214H.
[48] G. Haacke, New figure of merit for transparent conductors, J. Appl. Phys. 47 (1976) 4086–4089, https://doi.org/10.1063/1.323240.
[49] A. Anand, M.M. Islam, R. Meitzner, U.S. Schubert, H. Hoppe, Introduction of a novel figure of merit for the assessment of transparent conductive electrodes in photovoltaics: exact and approximate form, Adv. Energy Mater. 11 (2021), https://doi.org/10.1002/aenm.202100875.
[50] N. Lu, Z. Suo, J.J. Vlassak, The effect of film thickness on the failure strain of polymer-supported metal films, Acta Mater. 58 (2010) 1679–1687, https://doi.org/10.1016/j.actamat.2009.11.010.
[51] O. Glushko, M.J. Cordill, Electrical resistance of metal films on polymer substrates under tension, Exp. Tech. 40 (2016) 303–310, https://doi.org/10.1007/s40799-016-0040-x.
[52] O. Glushko, P. Kraker, M.J. Cordill, Explicit relationship between electrical and topological degradation of polymer-supported metal films subjected to mechanical loading, Appl. Phys. Lett 110 (2017) 1–5, https://doi.org/10.1063/1.4982802.
[53] O. Glushko, M. Mühlbacher, C. Gammer, M.J. Cordill, C. Mitterer, J. Eckert, Exceptional fracture resistance of ultrathin metallic glass films due to an intrinsic size effect, Sci. Rep. 9 (2019) 1–9, https://doi.org/10.1038/s41598-019-44384-z.
[54] L. Rebouta, L. Rubio-Peña, C. Oliveira, S. Lanceros-Mendez, C.J. Tavares, E. Alves, Strain dependence electrical resistance and cohesive strength of ITO thin films deposited on electroactive polymer, Thin Solid Films 518 (2010) 4525–4528, https://doi.org/10.1016/j.tsf.2009.12.022.
[55] T.S. Bejitual, N.J. Morris, D.R. Cairns, K.A. Sierros, Controlled buckling behavior of patterned oxide structures on compliant substrates for flexible optoelectronics, Thin Solid Films 549 (2013) 268–275, https://doi.org/10.1016/j.tsf.2013.05.173.
[56] C.S. Pande, K.P. Cooper, Nanomechanics of Hall-Petch relationship in nanocrystalline materials, Prog. Mater. Sci. 54 (2009) 689–706, https://doi.org/10.1016/j.pmatsci.2009.03.008.
[57] F. Ahmed, K. Bayerlein, S.M. Rosiwal, M. Göken, K. Durst, Stress evolution and cracking of crystalline diamond thin films on ductile titanium substrate: analysis by micro-raman spectroscopy and analytical modelling, Acta Mater. 59 (2011) 5422–5433, https://doi.org/10.1016/j.actamat.2011.05.015.
[58] P. Jin, X. Li, Correction of image drift and distortion in a scanning electron microscopy, J. Microsc. 260 (2015) 268–280, https://doi.org/10.1111/jmi.12293.
[59] L. Xu, T.C. Shyu, N.A. Kotov, Origami and Kirigami nanocomposites, ACS Nano 11 (2017) 7587–7599, https://doi.org/10.1021/acsnano.7b03287.
[60] O. Glushko, A. Klug, E.J.W.W. List-Kratochvil, M.J. Cordill, Relationship between mechanical damage and electrical degradation in polymer-supported metal films subjected to cyclic loading, Mater. Sci. Eng. A 662 (2016) 157–161, https://doi.org/10.1016/j.msea.2016.03.052.
[61] G.D. Sim, Y.S. Lee, S.B. Lee, J.J. Vlassak, Effects of stretching and cycling on the fatigue behavior of polymer-supported Ag thin films, Mater. Sci. Eng. A 575 (2013) 86–93, https://doi.org/10.1016/j.msea.2013.03.043.
[62] M.J. Cordill, O. Glushko, A. Kleinbichler, B. Putz, D.M. Többens, C. Kirchlechner, Microstructural influence on the cyclic electro-mechanical behaviour of ductile films on polymer substrates, Thin Solid Films 644 (2017) 166–172, https://doi.org/10.1016/j.tsf.2017.06.067.
[63] O. Glushko, B. Putz, M.J. Cordill, Determining effective crack lengths from electrical measurements in polymer-supported thin films, Thin Solid Films 699 (2020) 137906, https://doi.org/10.1016/j.tsf.2020.137906.
[64] J.S. Meena, S. Bin Choi, S.B. Jung, J.W. Kim, Advances in silver nanowires-based composite electrodes: materials processing, fabrication, and applications, Adv. Mater. Technol. 8 (2023) 1–43, https://doi.org/10.1002/admt.202300602.
[65] J. Wang, J. Fan, T. Wan, L. Hu, Z. Li, D. Chu, Recent progress in silver nanowire-based transparent conductive electrodes, Adv. Energy Sustain. Res (2025) 2500033, https://doi.org/10.1002/aesr.202500033.